Available online at www.sciencedirect.com

ScienceDirect

Journal of Computational Physics 220 (2007) 839–855

JOURNAL OF COMPUTATIONAL PHYSICS

www.elsevier.com/locate/jcp

Electromagnetic gyrokinetic δf particle-in-cell turbulence simulation with realistic equilibrium profiles and geometry

Yang Chen *, Scott E. Parker

Center for Integrated Plasma Studies, University of Colorado at Boulder, Boulder, CO 80309, United States

Received 25 March 2005; received in revised form 23 May 2006; accepted 24 May 2006
Available online 10 July 2006

Abstract

The δf particle-in-cell method for gyrokinetic simulations with kinetic electrons and electromagnetic perturbations [Y. Chen, S. Parker, J. Comput. Phys. 189 (2003) 463] is extended to include arbitrary toroidal equilibrium profiles and flux-surface shapes. The domain is an arbitrarily sized toroidal slice with periodicity assumed in toroidal direction. It is global radially and poloidally along the magnetic field. The differential operators and Jacobians are represented numerically which is a quite general approach with wide applicability. Discretization of the field equations is described. The issue of domain decomposition and particle load balancing is addressed. A derivation of the split-weight scheme is given, and numerical observations are given as to what algorithmic change leads to stable algorithm. It is shown that in the final split-weight algorithm the equation for the rate of change of the electric potential is solved in a way that is incompatible with the quasi-neutrality condition on the grid scale. This incompatibility, while negligible on the scale of interest, leads to better numerical stability on the grid scale. Some examples of linear simulations are presented to show the effects of flux-surface shaping on the linear mode growth rates. The issue of long-term weight growth in δf simulation and the effect of discrete particle noise are briefly discussed.

PACS: 52.65.+z; 52.35.Mw

Keywords: Gyrokinetic simulation; δf method; Generalized split-weight scheme; Electromagnetic turbulence; Flux-surface shape

1. Introduction

We present a method for extending electromagnetic δf particle-in-cell (PIC) gyrokinetic simulations [1] to general geometry, including equilibrium profile variations. At the present time gyrokinetic simulation of the electrostatic ion-temperature-gradient (ITG) modes and trapped-electron-modes (TEMs) with adiabatic electrons or with kinetic trapped electrons [2] has become a mature numerical tool for stability and transport analysis. Electromagnetic simulation with fully kinetic electrons, on the other hand, is much more difficult, and has become practical only recently. In a previous paper we have presented an electromagnetic δf particle algorithm

[*] Corresponding author. Tel.: +1 303 492 3664; fax: +1 303 492 0642.
E-mail address: yang.chen@colorado.edu (Y. Chen).

doi:10.1016/j.jcp.2006.05.028

for turbulence simulations [1]. The algorithm uses parallel momentum $p_\|$ instead of parallel velocity $v_\|$ as a coordinate to avoid the difficulty with evaluating the inductive component of the parallel electric field, $\partial A_\|/\partial t$. It uses the generalized split-weight scheme [3] to enhance the time step, and a modified Ampere equation to solve the accuracy problem at high β [4]. Validation of the algorithm includes benchmark with the dispersion relation in shearless slab geometry, and benchmark with the continuum code GS2 [5] and GYRO [6] in toroidal, flux-tube geometry. The GEM code is based on this algorithm, but has been recently extended to include general flux surface geometry and equilibrium profiles.

The constraint on the time step due to rapid electron motion along the field line is removed in the continuum codes GS2 and GYRO by treating the parallel streaming motion in the electron gyrokinetic equation implicitly. Implicit algorithm can also be used for particle simulation [7] to achieve large time steps. If the $v_\|$ formalism [8] is used and the inductive electric field $\partial A_\|/\partial t$ is also treated implicitly, the high-β accuracy problem with the Ampere's equation does not arise. Such an implicit scheme might in the future provide an alternative to the GEM algorithm for δf particle simulation.

The GEM algorithm is explicit. Its efficacy in increasing the time step has only been demonstrated numerically, and is not well understood. A prominent feature of the split-weight scheme is the extra field equation for the rate of change of the electric potential, $\dot{\phi}$. While in the continuum limit, i.e. with vanishing grid size and time step, and infinite number of particles, solving both the quasi-neutrality condition and the equation for $\dot{\phi}$ is redundant, the two equations are not consistent on the grid scale, due to the use of finite grid sizes. In this paper, we show that the key to the efficacy of the split-weight scheme is this inconsistency, which tends to suppress grid-scale numerical instabilities.

The rest of the paper is organized as follows. In Section 2, the extension to general equilibrium configuration in GEM is described. The split-weight scheme as used in GEM is analyzed in Section 3. Discretization and solution method for the field equations are described in Section 4. Examples of simulations in general geometry are given in Section 5. Concluding remarks are given in Section 6.

2. Representation of general equilibrium

In this section, we present details of how equilibrium quantities, such as the q-profile, the Jacobian, etc., are specified and represented in the simulations. The complete set of equations to be solved consists of the electron and ion gyrokinetic equations, the quasi-neutrality condition for the electric potential ϕ, the Ampere's equation for the vector potential $A_\|$, and the equation for the rate of change of ϕ, $\dot{\phi}$, as required by the split-weight scheme. We refer the readers to Ref. [1] for details regarding the split-weight scheme. Only those parts of the simulation that are modified by general geometry will be discussed here.

The equilibrium magnetic field in a axisymmetric toroidal plasma is given by

$$\mathbf{B} = \mathbf{B}_\mathrm{t} + \mathbf{B}_\mathrm{p} = \frac{f(\Psi)}{R}\hat{\zeta} + \nabla\zeta \times \nabla\Psi. \tag{1}$$

Here $\Psi(R,Z)$ is the poloidal flux function, $f(\Psi)$ is an arbitrary flux function, $\mathbf{B}_\mathrm{t}$ the toroidal field, $\mathbf{B}_\mathrm{p}$ the poloidal field, (R,Z,ζ) are a set of right-handed cylindrical coordinates with R the major radius. These are related to the generalized toroidal coordinates (r,θ,ζ) through $R = R(r,\theta)$ and $Z = Z(r,\theta)$. Here r is a radius-like coordinate which is also a flux label, $\Psi = \Psi(r)$, and θ is a "poloidal angle" with periodicity 2π. Equilibrium is more conveniently specified by the safety factor $q(r)$ instead of $\Psi(r)$. By definition, $\mathrm{d}\Psi = 2\pi R B_\mathrm{p}\mathrm{d}\rho(l)$ where l is the poloidal arc length along the magnetic surface Ψ and $\mathrm{d}\rho(l)$ is the normal distance between the magnetic surfaces Ψ and $\Psi + \mathrm{d}\Psi$, which depends on the poloidal angle hence l. The toroidal flux through the annulus $\mathrm{d}\Psi$ is

$$\mathrm{d}\chi = \oint \mathrm{d}\rho(l)\frac{f}{R}\mathrm{d}l = \mathrm{d}\Psi\frac{f}{2\pi}\oint\frac{\mathrm{d}l}{R^2 B_\mathrm{p}}, \tag{2}$$

hence

$$q(\Psi) = \mathrm{d}\chi/\mathrm{d}\Psi = \frac{f}{2\pi}\oint\frac{\mathrm{d}l}{R^2 B_\mathrm{p}}. \tag{3}$$

The line element $\mathrm{d}l$ is related to $\mathrm{d}\theta$ through $\mathrm{d}l = \mathrm{d}\theta|\nabla\Psi|/|\nabla\Psi\times\nabla\theta|$, therefore

$$\oint \mathrm{d}\theta \frac{f}{Rq|\nabla\Psi\times\nabla\theta|} = 2\pi. \tag{4}$$

Once the flux surface shape $R(r,\theta)$ and $Z(r,\theta)$ and the q-profile is given, Eq. (4) can be used to define $\Psi(r)$. The poloidal field B_p is then computed from Eq. (1). A general equilibrium can only be represented numerically, e.g. B_p can be represented by a two-dimensional numerical table. In this paper the Miller equilibrium are used to generate those numerical tables. The flux surfaces for the Miller model are given by [9]

$$R = R_0(r) + r\cos(\theta + \arcsin\delta(r))\sin\theta, \tag{5}$$

$$Z = \kappa(r) r \sin\theta. \tag{6}$$

The Miller equilibrium model is a local equilibrium model, which satisfies the Grad–Shafronov equation. Given the shape of a flux surface and other local parameters (such as the safety factor q, elongation and triangularity, etc.) the Miller model also provides a complete specification for the local magnetic field, which determines the drift motion locally. Thus the flux function $f(\Psi)$ in Eq. (1) is locally determined from the given flux-surface shape and local parameters [9]. In a global simulation the global model for the flux-surface shape, Eqs. (5) and (6), with arbitrary radial dependence of R_0, κ and δ, cannot be made to satisfy the Grad–Shafronov equation. We therefore only use Eqs. (5) and (6) to specify the flux surface shapes, and adopt the view that the flux function $f(\Psi)$ is to be specified separately, e.g. from experimental data on the toroidal magnetic field strength. In GEM the main code only assumes a given general toroidal coordinates (r,θ,ζ) and equilibrium quantities such as B, q defined on (r,θ) grids. Defining the mapping $(X,Z)\to(r,\theta)$ and computing the equilibrium quantities are done in an "equilibrium module". Unnecessary assumption on the equilibrium configuration is avoided by this encapsulation of the equilibrium.

2.1. Normalization

We consider a toroidal plasma with an on-axis magnetic field strength of B_0, ion temperature $T_{0\mathrm{i}}$, electron temperature $T_{0\mathrm{e}}$ and ion number density n_0 at the center of the simulation domain. B_0 is used as unit for measuring magnetic field strength and n_0 for number density. We assume ions are singly charged. The ion mass and electron mass are measured in units of the proton mass, m_p, and are denoted by m_i and m_e. Defining $m_\mathrm{p}v_\mathrm{u}^2 = T_{0\mathrm{i}}$ and $x_\mathrm{u} = \sqrt{m_\mathrm{p}T_{0\mathrm{i}}}/eB_0$, v_u is used as the unit for velocity, x_u the unit for length, and time is measured in unit of $t_\mathrm{u} = m_\mathrm{p}/eB_0$. Finally, we define $m_\mathrm{i}v_{T\mathrm{i}}^2 = 1$ and $m_\mathrm{e}v_{T\mathrm{e}}^2 = T_{0\mathrm{e}}/T_{0\mathrm{i}} = 1/\tau$, so that electric potential ϕ, vector potential $A_\parallel$ and electric current are measured in units of $T_{0\mathrm{i}}/e$, $T_{0\mathrm{i}}/ev_\mathrm{u}$ and en_0v_u, respectively.

2.2. Equation of motion in the field-line-following coordinates

The field-line-following coordinates are defined in terms of the toroidal coordinates:

$$x = r - r_0, \tag{7}$$

$$y = \frac{r_0}{q_0}\left(\int_0^\theta \mathrm{d}\theta\hat{q}(r,\theta) - \zeta\right), \tag{8}$$

$$z = q_0 R_\mathrm{maj}\theta, \tag{9}$$

here r_0 is a reference radius, $q_0 = q(r_0)$, R_maj is the major radius of the magnetic axis. $\hat{q}(r,\theta) = \frac{\mathbf{B}\cdot\nabla\zeta}{\mathbf{B}\cdot\nabla\theta}$. The coordinates (x,y) are chosen such that $\mathbf{B}\cdot\nabla x = \mathbf{B}\cdot\nabla y = 0$. With this choice of y coordinate the toroidal boundary condition is the same as in the flux-tube case [10], i.e. the θ value jumps by 2π in Eq. (8) and the jump in y is computed accordingly.

Equation of motion is obtained from $\dot{x} = \mathbf{V}_G\cdot\nabla x$, etc., where $\mathbf{V}_G = v_\parallel\tilde{\mathbf{b}} + \mathbf{v}_D + \mathbf{v}_E$ is the guiding-center velocity. Here $\tilde{\mathbf{b}} = \mathbf{b} + \frac{\langle\delta\mathbf{B}_\perp\rangle}{B}$, $\mathbf{v}_D = \frac{m(v_\parallel^2 + v_\perp^2/2)}{qB^3}\mathbf{B}\times\nabla B$ is the drift velocity, $\mathbf{v}_E = \langle\mathbf{E}\rangle\times\mathbf{b}/B$. $\langle\cdots\rangle$ stands for gyro-averaging. For clarity, we will suppress the species index. The guiding center motion is given by,

$$\mathbf{v}_D \cdot \nabla x = -\frac{e_B}{B^2}\frac{f}{R}\frac{\partial B}{\partial \theta}|\nabla r \times \nabla\theta|, \tag{10}$$

$$\mathbf{v}_D \cdot \nabla y \approx e_B \frac{f}{R}|\nabla r \times \nabla\theta|\left(-\frac{\partial y}{\partial r}\frac{\partial B}{\partial \theta} + \hat{s}\frac{\partial B}{\partial r}\right), \tag{11}$$

$$v_\parallel \mathbf{b} \cdot \nabla z = \frac{v_\parallel q_0 R_{\mathrm{maj}}}{BR}\Psi'(r)|\nabla r \times \nabla\theta|, \tag{12}$$

$$\mathbf{v}_E \cdot \nabla x = \hat{s}\frac{\langle E_y \rangle}{B^2}\frac{f}{R}|\nabla r \times \nabla\theta|, \tag{13}$$

$$\mathbf{v}_E \cdot \nabla y = -\hat{s}\frac{\langle E_x \rangle}{B^2}\frac{f}{R}|\nabla r \times \nabla\theta|, \tag{14}$$

$$\mathbf{v}_E \cdot \nabla z \approx 0, \tag{15}$$

with $e_B = m(v_\parallel^2 + v_\perp^2/2)/qB$, $\hat{s}(r,\theta) = \frac{r_0}{q_0}\hat{q}$, $E_x = -\frac{\partial\phi}{\partial x}$, $E_y = -\frac{\partial\phi}{\partial y}$ and $E_z = -\frac{\partial\phi}{\partial z}$. Expressions for the field line bending term, $v_\parallel \delta\mathbf{B}_\perp/B$, can be obtained using the vector potential $A_\parallel$ similar to $\mathbf{v}_E$. The mirror force is given by

$$\dot{v}_\parallel = -\frac{\mu}{m}\mathbf{b} \cdot \nabla B = -\frac{\mu}{mRB}\Psi'(r)\frac{\partial B}{\partial \theta}|\nabla r \times \nabla\theta|. \tag{16}$$

Quantities such as $\frac{\partial y}{\partial r}$, $\frac{\partial B}{\partial r}$, $\frac{\partial B}{\partial \theta}$ and $|\nabla r \times \nabla\theta|$ are all computed and saved as numerical tables.

Gyro-averaging for the perturbed quantities $\langle E_x \rangle$, etc., is done using the four-point averaging scheme [11]. The location of the four points, $\mathbf{r}(x + \Delta x_l, y + \Delta y_l)$, $l = (1,2,3,4)$, are obtained from

$$\mathbf{r}(x + \Delta x_l, y + \Delta y_l) - \mathbf{r}(x,y) \approx \frac{\partial \mathbf{r}}{\partial x}\Delta x_l + \frac{\partial \mathbf{r}}{\partial y}\Delta y_l = \boldsymbol{\rho}_l. \tag{17}$$

Here $\boldsymbol{\rho}_l$ is the vector leading from the guiding center to the particle position on its gyro-ring. Setting $\boldsymbol{\rho}_1 = \rho\hat{\mathbf{r}}$, $\boldsymbol{\rho}_2 = -\rho\hat{\mathbf{r}}$, $\boldsymbol{\rho}_3 = \rho\mathbf{b} \times \hat{\mathbf{r}}$ and $\boldsymbol{\rho}_4 = -\rho\mathbf{b} \times \hat{\mathbf{r}}$, with $\hat{\mathbf{r}} = \nabla r/|\nabla r|$, one obtains,

$$\Delta x_1 = \rho|\nabla r|, \tag{18}$$

$$\Delta y_1 = \rho\nabla x \cdot \nabla y/|\nabla r|, \tag{19}$$

$$\Delta x_2 = -\Delta x_1, \tag{20}$$

$$\Delta y_2 = -\Delta y_1, \tag{21}$$

$$\Delta x_3 = 0, \tag{22}$$

$$\Delta y_3 = \frac{\rho}{B|\nabla r|}\left(\hat{s}\frac{f}{R}|\nabla r \times \nabla\theta| + \frac{r_0\Psi'}{q_0 R^2}|\nabla r|^2\right), \tag{23}$$

$$\Delta x_4 = 0, \tag{24}$$

$$\Delta y_4 = -\Delta y_3. \tag{25}$$

2.3. Modification due to the Jacobian

The simulation domain is given by $(0, L_x) \times (0, L_y) \times (0, L_z)$ with $L_z = 2\pi q_0 R_{\mathrm{maj}}$, which is divided into $N_x \times N_y \times N_z$ equally sized cells in (x,y,z) coordinates. For a strongly shaped plasma the jacobian

$$J = (\nabla x \cdot \nabla y \times \nabla z)^{-1} \tag{26}$$

can be significantly different from unity. Marker particles are typically loaded according to the physical equilibrium distribution, which, in this paper, is assumed to be Maxwellian. It is clear then that the markers can be strongly nonuniform in (x,y,z) space. Since the perturbed density and current on a grid indexed (i,j,k) are computed by summing over particles nearby grid (i,j,k), the nonuniformity of markers at different grid points should be accounted for. More precisely, for any Y among $(1, v_\parallel, \dot{x}, \dot{y}, \dot{z})$,

$$\int Y\tilde{f}\,\mathrm{d}\mathbf{v} \approx \frac{N}{V}\sum_j \frac{1}{\Delta V_j} w_j Y_j S(\mathbf{x}-\mathbf{x}_j). \tag{27}$$

Here w_j is the particle weight, $\Delta V_j = J(\mathbf{x}_j)\Delta x\Delta y\Delta z$, $V = \sum_{\text{grids}}\Delta V$ is the total volume. N is the total number of marker particles of the species. $S(\mathbf{x}-\mathbf{x}_j) = S_{1\text{D}}(x/\Delta x)S_{1\text{D}}(y/\Delta y)S_{1\text{D}}(z/\Delta z)$ is the particle shape function with

$$S_{1\text{D}}(x) = \begin{cases} 1-|x| & \text{for } |x| \leqslant 1, \\ 0 & \text{for } |x| > 1. \end{cases} \tag{28}$$

The perturbed density is obtained with $Y = 1$, parallel current with $Y = v_\parallel$. Moments of the distribution with $Y = (\dot{x}, \dot{y}, \dot{z})$ are needed to compute the rate of change of the charge density in the equation for $\dot{\phi}$.

2.4. Equilibrium flow

The presence of equilibrium flow of large magnitude and large gradients ($V \sim v_{T\text{i}}$, $L_E \sim \rho_{\theta\text{i}}$ where L_E is the scale length of the equilibrium electric field and $\rho_{\theta\text{i}}$ is the poloidal gyro-radius) generally requires extension to the gyrokinetic formalism commonly used in simulations [12]. Here we consider only flows of subsonic magnitude ($\ll v_{T\text{i}}$) with longer scale length ($\sim a$). The dominant effects of such sheared flows can be accounted for without substantial modification of the equations. Consider an equilibrium electric potential $\Phi_0(r)$, of the same order as ϕ. The $E\times B$ motion due to Φ_0 is implemented as an additional term in Eq. (14). More care is needed to derive the particle weight equation. In the presence of Φ_0 the equilibrium distribution depends on $mv^2/2 + q\Phi_0$, hence in the $p_\parallel$ formulation of the δf method ($p_\parallel = v_\parallel + (q/m)A_\parallel$) we choose the zero-order distribution to be $f_0(\varepsilon, \mu, \mathbf{x})$, with $\varepsilon = \frac{1}{2}m(v_\perp^2 + p_\parallel^2) + q\Phi_0$. f_0 satisfies the equilibrium kinetic equation, written in terms of $p_\parallel$,

$$(p_\parallel \mathbf{b} + \mathbf{v}_D + \mathbf{v}_{E0})\cdot\nabla f_0 = 0. \tag{29}$$

The gradient operator acts on f_0 with ε and μ fixed. The perturbed distribution $\delta f = f - f_0$ evolves according to

$$\dot{\delta f} = -\left(\mathbf{v}_E + v_\parallel\frac{\langle\delta\mathbf{B}_\perp\rangle}{B}\right)\cdot\nabla f_0 - \dot{\varepsilon}\frac{\partial f_0}{\partial\varepsilon}. \tag{30}$$

Noticing that part of the equilibrium density gradient is implicit in $\Phi_0(r)$, we make a change of variable from ε to the particle kinetic energy $\varepsilon_\text{p} = \frac{1}{2}m(v_\perp^2 + p_\parallel^2)$. This gives

$$\dot{\delta f} = -\left(\mathbf{v}_E + v_\parallel\frac{\langle\delta\mathbf{B}_\perp\rangle}{B}\right)\cdot\nabla f_0 - \left(\dot{\varepsilon} - q\left(\mathbf{v}_E + v_\parallel\frac{\langle\delta\mathbf{B}_\perp\rangle}{B}\right)\cdot\nabla\Phi_0\right)\frac{\partial f_0}{\partial\varepsilon_\text{p}}, \tag{31}$$

where the gradient operator acts with ε_p fixed. The first term on the right-hand-side (r.h.s.) gives the conventional ω^* term with isotropic f_0 and $\Phi_0 = 0$. The coefficient of $\partial f_0/\partial\varepsilon_\text{p}$ can be easily evaluated,

$$\dot{\varepsilon}_\text{p} \equiv \dot{\varepsilon} - q\left(\mathbf{v}_E + v_\parallel\frac{\langle\delta\mathbf{B}_\perp\rangle}{B}\right)\cdot\nabla\Phi_0 = -q(v_\parallel\mathbf{b} + \mathbf{v}_D)\cdot\nabla\phi + qv_\parallel(v_\parallel\mathbf{b} + \mathbf{v}_D)\cdot\nabla A_\parallel + q\dot{p}_\parallel A_\parallel. \tag{32}$$

And δf evolves according to

$$\dot{\delta f} = \left(\mathbf{v}_E + v_\parallel\frac{\langle\delta\mathbf{B}_\perp\rangle}{B}\right)\cdot\boldsymbol{\kappa} f_0 + \frac{\dot{\varepsilon}_\text{p}}{T}f_0 \tag{33}$$

with $\boldsymbol{\kappa} = -\nabla f_0/f_0$. Notice that $\dot{\varepsilon}_\text{p}$ is not the rate of change of ε_p along the particle trajectory. The latter includes an additional term $-q\mathbf{v}_D\cdot\nabla\Phi_0$. At this point f_0 can be taken as a simple Maxwellian with density $n_0(r)$ and temperature $T(r)$. In this paper we keep only the $E\times B$ nonlinearity and the field line bending nonlinearity, so that nonlinear terms in the particle weight equation are neglected. Thus we keep only the mirror force, Eq. (16), in $\dot{p}_\parallel$, and $v_\parallel$ in the above expression can be replaced with $p_\parallel$. We also neglect the parallel nonlinearity term in the gyrokinetic equation ($\dot{v}_\parallel\partial\delta f/\partial v_\parallel$), to ensure that the marker distribution in the velocity space remain close to the assumed form (usually a Maxwellian distribution) at all times. This is required for the δf method to be valid. However, the marker distribution can in principle deviate from the assumed distribution if particles are subject to parallel acceleration. This is particularly worrisome for electrons because of the small electron mass. To accurately study the effect of parallel nonlinearity in the long term it is necessary to monitor the marker distribution and develop procedures (such as a proper collision operator) to ensure the assumed form for the marker distribution. Because we do not have such a capability yet, the parallel nonlinearity is simply neglected in this paper.

Equilibrium parallel flow of small magnitude ($V_\parallel \ll v_{T\mathrm{i}}$), which is important in the core of tokamaks, can be accounted for by choosing the appropriate μ dependence of f_0.

3. The split-weight scheme

The split-weight scheme is a technique to handle the fast electron parallel motion. It is so named because the electron distribution δf_e is split as

$$\delta f_\mathrm{e} = -\varepsilon_g \phi \frac{\partial f_{0\mathrm{e}}}{\partial \varepsilon_\mathrm{p}} + h, \tag{34}$$

where ε_g a free parameter. Only the distribution h is represented by the particle weights and simulated. A complete understanding of the split-weight scheme is lacking. The original argument [13] for adopting the split-weight scheme is that, with $\varepsilon_g = 1$, the first term in Eq. (34) catches the adiabatic response of the electrons, which well approximates the electron response in the limit $\omega/k_\parallel v_{T\mathrm{e}} \ll 1$. Since the dominant effect of the fast streaming is analytically represented, larger time steps should be possible for the simulation of h. As previously pointed out [3], this argument is only partially relevant. Firstly, trapped electrons are far from being adiabatic in a tokamak. Secondly, one does not have to choose $\varepsilon_g = 1$ to achieve enhancement of time steps, even for the problem of electrostatic ITG in a shearless slab where adiabatic electron response is a good approximation. In practice we often use $\varepsilon_g = 0.1$. It is not clear at all why such a small ε_g should dramatically increase the numerical stability. Thirdly, with magnetic fluctuations the adiabatic response is proportional to $(\phi - v_\parallel A_\parallel)$, but the scheme for splitting the distribution, Eq. (34), need not be modified.

The following discussion is an attempt to find the crucial steps in the split-weight scheme that lead to better numerical stability. While finding out these steps does not by itself constitute a proof of numerical stability, we hope the information will be useful for future analysis of the split-weight scheme.

The discretization of the equation for $\dot{\phi} = \partial\phi/\partial t$ is previously obtained from the continuity form of the gyrokinetic equation [3]. This approach, while leading to the correct form of the final scheme used in GEM, does not show where alternative schemes can arise. In this section, we present a derivation of the numerical scheme, and in doing so indicate where difference arises between the ways grid-scale numerical modes are treated differently in the split-weight scheme and conventional δf method. A prominent feature of the split-weight scheme is that a field equation for the quantity $\dot{\phi}$, is solved, in addition to the quasi-neutrality condition for ϕ. While on the scale of interest the algorithm is carefully constructed so that the two equations for ϕ and $\dot{\phi}$ are redundant, on the grid scale the two equations are incompatible, also by construction. Numerical instabilities that arise due to parallel electron motion have short parallel wavelengths, hence are more sensitive to such grid-scale incompatibility. The equation for $\dot{\phi}$ has been previously derived from the quasi-neutrality condition prior to its discretization, which, while strictly correct, does not show explicitly how a different treatment of the grid-scale modes arises. It is instructive then to derive the $\dot{\phi}$ equation directly from the discretized Poisson equation.

The electron weight $w = h/f_{0\mathrm{e}}$ evolves according to

$$\frac{\mathrm{d}w}{\mathrm{d}t} = -\left(\mathbf{v}_E + v_\parallel \frac{\delta \mathbf{B}_\perp}{B}\right) \cdot \boldsymbol{\kappa} - \dot{\varepsilon}_\mathrm{p} + \varepsilon_g \frac{\mathrm{d}\phi}{\mathrm{d}t}. \tag{35}$$

Here $\dot{\varepsilon}_\mathrm{p}$ is given by Eq. (32),

$$\frac{\mathrm{d}\phi}{\mathrm{d}t} = \frac{\partial\phi}{\partial t} + \dot{x}\frac{\partial\phi}{\partial x} + \dot{y}\frac{\partial\phi}{\partial y} + \dot{z}\frac{\partial\phi}{\partial z} = \frac{\partial\phi}{\partial t} + \mathbf{v}_G \cdot \nabla\phi. \tag{36}$$

The quasi-neutrality condition is

$$n_\mathrm{p} + \varepsilon_g \tau \frac{V}{N} \sum_j \frac{1}{\Delta V_j} \phi(\mathbf{x}_j, t) S(\mathbf{x} - \mathbf{x}_j) = -\frac{V}{N} \sum_j \frac{1}{\Delta V_j} w_j S(\mathbf{x} - \mathbf{x}_j) + \text{ion term}. \tag{37}$$

Here n_p is the ion polarization density, $S(\mathbf{x})$ is the particle shape function used to deposit particle quantities on the grids. This equation differs from Eq. (10) of Ref. [1] in that the $\varepsilon_g\tau\phi$ term is also discretized. Now an equation for $\dot{\phi}$ that is numerically compatible with Eqs. (35) and (37) can be derived by taking the time derivative of Eq. (37) (with $\mathbf{x}$ fixed). Assuming for the moment S is smooth,

$$\begin{aligned}\dot{n}_\mathrm{p} = {} & \frac{V}{N}\sum_j \frac{1}{\Delta V_j}\left(\left(\mathbf{v}_E + v_\parallel \frac{\delta \mathbf{B}_\perp}{B}\right)_j \cdot \boldsymbol{\kappa}_j + \dot{\varepsilon}_{pj}\right) S(\mathbf{x}-\mathbf{x}_j) \\ & + \frac{V}{N}\sum_j \frac{1}{\Delta V_j}(w_j + \varepsilon_g\tau\phi(\mathbf{x}_j,t))\mathbf{v}_{Gj}\cdot\nabla S(\mathbf{x}-\mathbf{x}_j) + \text{ion terms},\end{aligned} \tag{38}$$

using $\frac{\mathrm{d}}{\mathrm{d}t}(\phi S(\mathbf{x}-\mathbf{x}_j)) = \frac{\mathrm{d}\phi}{\mathrm{d}t}S - \phi\mathbf{v}_G\cdot\nabla S$ and $\frac{\mathrm{d}\phi}{\mathrm{d}t} = \frac{\partial}{\partial t}\phi(\mathbf{x}_j,t) + \mathbf{v}_{Gj}\cdot\frac{\partial}{\partial \mathbf{x}_j}\phi(\mathbf{x}_j,t)$. In Eq. (38) $\dot{n}_\mathrm{p} = \sum_\mathbf{k}(1-\Gamma_0(b))\dot{\phi}_\mathbf{k}\exp(\mathrm{i}\mathbf{k}\cdot\mathbf{x})$. Notice that the gradient operator ∇ acts w.r.t. $\mathbf{x}$ and gradient w.r.t. particle position $\mathbf{x}_j$ is written as a fraction. The second term on the r.h.s. of Eq. (38) is ill-defined if the nearest-grid-point scheme is used for S. If no particles are exactly located at the middle of a grid cell in any dimension, this term is zero, otherwise it is infinity. For the case of linear interpolation, $S(\mathbf{x}-\mathbf{x}_j)$ is piece-wise linear and ∇S can be defined also piece-wise. Then Eq. (38) does yield a plausible scheme for gathering the source terms of the $\dot{\phi}$ equation. We have indeed tested this scheme for the second term on the r.h.s. of Eq. (38), which causes numerical instabilities. Eq. (38) differs from the actual gathering scheme for the source terms of the $\dot{\phi}$ equation in the following three aspects.

(a) Firstly, the second term on the r.h.s. is written as

$$\frac{V}{N}\sum_j \frac{1}{\Delta V_j}(w_j + \varepsilon_g\tau\phi(\mathbf{x}_j,t))\mathbf{v}_{Gj}\cdot\nabla S(\mathbf{x}-\mathbf{x}_j) = \frac{V}{N}\nabla\cdot\sum_j \frac{1}{\Delta V_j}(w_j + \varepsilon_g\tau\phi(\mathbf{x}_j,t))\mathbf{v}_{Gj}S(\mathbf{x}-\mathbf{x}_j). \tag{39}$$

This is allowed since the differential operators act in $\mathbf{x}$ space. To see the effect of this procedure, we evaluate both sides of Eq. (39) in the continuum limit. Since numerical instability is associated with only the parallel motion, we consider only the z direction. Linear interpolation corresponds to

$$\frac{\partial}{\partial z}S_{1\mathrm{D}}\left(\frac{z-z_j}{\Delta z}\right) = \begin{cases} 1/\Delta z & \text{for } |z-z_j|/\Delta z \leqslant 1,\ z \leqslant z_j, \\ -1/\Delta z & \text{for } |z-z_j|/\Delta z \leqslant 1,\ z > z_j, \\ 0 & \text{for } |z-z_j|/\Delta z > 1. \end{cases} \tag{40}$$

To evaluate a discrete sum over particles in the large particle number limit we need the following prescription for converting a velocity moment of f_0 to discrete sum and vice versa:

$$\int(\cdots)f_0\,\mathrm{d}\mathbf{v} = \frac{V}{N}\sum_j \frac{1}{\Delta V_j}(\cdots)_j S(\mathbf{x}-\mathbf{x}_j). \tag{41}$$

Then, for any Fourier component $\phi(z_j) = \phi_k\exp(\mathrm{i}kz_j)$ and $w_j = h(p_{\parallel j})\exp(\mathrm{i}kz_j)$, we have

$$\frac{V}{N}\sum_j \frac{1}{\Delta V_j}(w_j + \varepsilon_g\tau\phi(z_j))p_\parallel\frac{\partial S}{\partial z} = \mathrm{i}k\mathrm{e}^{\mathrm{i}kz}C_1(k\Delta z)\int f_0(p_\parallel)(h + \varepsilon_g\tau\phi_k)\,\mathrm{d}p_\parallel, \tag{42}$$

$$C_1(x) = \frac{1}{x^2}(2 - 2\cos x), \tag{43}$$

and

$$\frac{V}{N}\frac{\partial}{\partial z}\sum_j \frac{1}{\Delta V_j}(w_j + \varepsilon_g\tau\phi(z_j))p_\parallel S = \mathrm{i}k\mathrm{e}^{\mathrm{i}kz}C_2(k\Delta z)\int f_0(p_\parallel)(h + \varepsilon_g\tau\phi_k)\,\mathrm{d}p_\parallel, \tag{44}$$

$$C_2(x) = \frac{1}{x^3}(2\sin x - \sin(2x)). \tag{45}$$

In Eq. (44) a spatially centered, 2-point, finite difference scheme is assumed for $\partial/\partial z$, i.e. $\partial f/\partial z = (f(z+\Delta z) - f(z-\Delta z))/(2\Delta z)$. We first notice that, an important conclusion regarding the split-weight scheme can be immediately drawn. Since C_2 is purely real, no numerical dissipation is introduced by using Eq. (39).

An example of numerical scheme for the left-hand-side (l.h.s.) of Eq. (44) with numerical dissipation is to use a dissipative difference scheme for $\partial/\partial z$, in which case C_2 has an imaginary part. In Fig. 1 are plotted the coefficients C_1 and C_2. For waves of physical interest with $k\Delta z \ll 1$ $C_2 \approx 1$, hence $\partial/\partial z \rightarrow ik$ from Eq. (44) as is required. On the other hand, for grid-scale waves with $k\Delta z \sim 1$, $C_2 \ll C_1$, in particular, at the shortest scale $k\Delta z = \pi$, $C_2 = 0$.

(b) Secondly, terms that vanish in the limit of infinite particle number are dropped. These include the $p_{\|}\delta\mathbf{B}_{\perp}$ term and the $\phi p_{\|}\mathbf{b}\cdot\nabla S$ term in Eq. (38), due to the fact that the marker particle distribution is even in $p_{\|}$. Noise from finite number of particles is thus reduced.

(c) Finally, there is another change associated with the magnetic perturbations. Recall Eq. (32), the $\dot{\varepsilon}_{\mathrm{p}}$ term in Eq. (38) contributes the following expression proportional to $A_{\|}$,

$$-e\frac{V}{N}\sum_j \frac{1}{\Delta V_j}\left(p_{\|j}(p_{\|}\mathbf{b}+\mathbf{v}_D)_j\cdot\frac{\partial}{\partial \mathbf{x}_j}A_{\|}(\mathbf{x}_j)+\dot{p}_{\|j}A_{\|}(\mathbf{x}_j)\right)S(\mathbf{x}-\mathbf{x}_j). \tag{46}$$

On the other hand, the continuum form of this contribution is obtained by directly integrating the corresponding terms in Eq. (33), i.e.

$$-e\frac{1}{T_{\mathrm{e}}}\int \mathrm{d}\mu\,\mathrm{d}p_{\|}\left(p_{\|}(p_{\|}\mathbf{b}+\mathbf{v}_D)\cdot\nabla A_{\|}+\dot{p}_{\|}A_{\|}\right)(f_0J'), \tag{47}$$

where J' is the Jacobian for the velocity space transformation, $2\pi v_{\perp}\mathrm{d}v_{\perp}\mathrm{d}p_{\|} = J'\mathrm{d}\mu\mathrm{d}p_{\|} = (2\pi B/m)\mathrm{d}\mu\mathrm{d}p_{\|}$. The equilibrium motion satisfies the incompressibility condition,

$$\nabla\cdot\left(J'(p_{\|}\mathbf{b}+\mathbf{v}_D)\right) = 0, \tag{48}$$

here the gradient is taken with μ and $p_{\|}$ fixed. Using Eqs. (48), (47) can be cast into the following form,

$$\begin{aligned}-e\frac{1}{T_{\mathrm{e}}}\nabla\cdot\int \mathrm{d}\mu\,\mathrm{d}p_{\|}p_{\|}(p_{\|}\mathbf{b}+\mathbf{v}_D)A_{\|}(f_0J') &= -\frac{e}{T_{\mathrm{e}}}\nabla\cdot\int \mathrm{d}\mu\,\mathrm{d}p_{\|}p_{\|}^2A_{\|}(f_0J')\mathbf{b}\\ &= -\frac{e}{T_{\mathrm{e}}}\frac{V}{N}\nabla\cdot\sum_j\frac{1}{\Delta V_j}p_{\|j}^2A_{\|}(\mathbf{x}_j)S(\mathbf{x}-\mathbf{x}_j)\mathbf{b},\end{aligned} \tag{49}$$

where the third line follows from discretization. Numerically we have observed that using Eq. (46) leads to numerical instability even for moderate β, while using Eq. (49) does not.

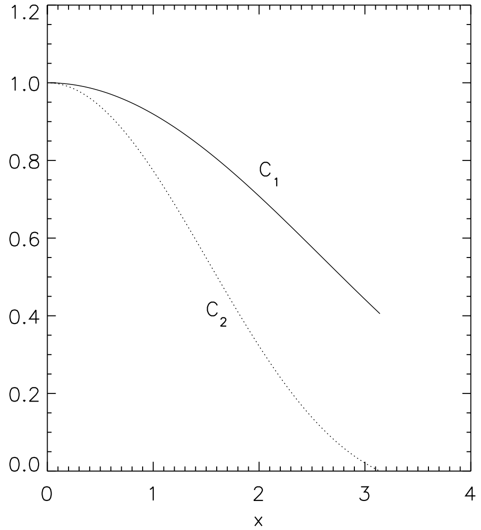

Fig. 1. The coefficients C_1 and C_2, showing large difference at the grid-scale.

The discretization schemes Eqs. (39) and (49) are naturally obtained if one starts with the continuity form of the gyrokinetic equation [3]. What we have shown in this Section is how these schemes differ from that strictly compatible with the Poisson equation at the grid scales. While revealing this difference between the conventional δf method and the split-weight scheme says nothing about the stability of the grid-scale modes in either scheme, such incompatibility apparently causes the split-weight scheme to be more stable numerically, as is indicated above. We also observed that only a small split-weight parameter, $\varepsilon_g \ll 1$, is needed for much improved numerical stability. This fact can be understood as follows. Without the split-weight scheme numerical instabilities with large $k_\parallel$ and small $k_\perp$ first develop as the time step is increased. Heuristically if $\varepsilon_g \sim k_\perp^2\rho_\mathrm{i}^2$ is used in the split-weight scheme, then the split-weight term in the quasi-neutrality condition (the second term in Eq. (37)) is comparable to the polarization term, and the numerically unstable Fourier component is strongly affected by enforcing the $\partial\phi/\partial t$ equation, which is incompatible with the quasi-neutrality condition for large $k_\parallel$ components. Thus with a box size with a fundamental mode of $k_\perp\rho_\mathrm{i} = 0.1$, a split-weight parameter of $\varepsilon_g = 0.05$ enhances the time step by several times, to a practically acceptable level, $\omega_\mathrm{ci}\Delta t = 2$.

4. Discretization of the field equations

In Ref. [1] the field equations are solved using fast Fourier transform (FFT), assuming periodic boundary conditions in x and y. This is only suitable for a local, flux-tube simulation. Discretization of the field equations for radially global simulations, and parallelization schemes (domain decomposition), are presented in this section.

4.1. Ampere's equation

The Ampere's equation is

$$-\nabla_\perp^2 A_\parallel + \beta_\mathrm{i}\hat{F}A_\parallel = \beta_\mathrm{i} j_\parallel, \tag{50}$$

with

$$\hat{F}A_\parallel \equiv \frac{V}{N}\sum_j \frac{1}{\Delta V_j} p_{\parallel j}^2 A_\parallel(\mathbf{x}_j) S(\mathbf{x}-\mathbf{x}_j), \tag{51}$$

$$A_\parallel(\mathbf{x}_j) = \sum_{l,m,n} A_{\parallel,lmn} S(\mathbf{x}_{lmn}-\mathbf{x}_j). \tag{52}$$

In Eq. (52) the subscript (l,m,n) is the spatial grid index. A suitable discretization for the differential operator $\nabla_\perp^2$ in Eq. (50) is understood, so that Eq. (50) can be viewed as a set of algebraic equations for the quantities $A_{\parallel,lmn}$. Let $g = (l,m,n)$,

$$\begin{aligned}\sum_g A_{\parallel,g}(\hat{F}A_\parallel)_g &= \frac{V}{N}\sum_j \frac{1}{\Delta V_j} p_{\parallel j}^2 \sum_g \sum_{g'} A_{\parallel,g} A_{\parallel,g'} S(\mathbf{x}_g-\mathbf{x}_j) S(\mathbf{x}_{g'}-\mathbf{x}_j)\\ &= \frac{V}{N}\sum_j \frac{1}{\Delta V_j} p_{\parallel j}^2 \left(\sum_g A_{\parallel,g} S(\mathbf{x}_g-\mathbf{x}_j)\right)^2.\end{aligned} \tag{53}$$

Hence the operator $\hat{F}$ is positive definite and Eq. (50) is well posed. Unlike the operator $\nabla_\perp^2$, which is a differential operator only in the (x,y)-plane, the operator $\hat{F}$ brings in the values of $A_\parallel$ at neighboring z grids. Moreover, $\hat{F}$ is dependent on the electron coordinates, so the inverse of $-\nabla_\perp^2 + \beta_\mathrm{i}\hat{F}$ need be constructed at each time step if a direct solver is pursued. In Ref. [1] the following iterative scheme is used,

$$\left(-\nabla_\perp^2 + \beta_\mathrm{i}\frac{m_\mathrm{p}}{m_\mathrm{e}}\right)A_\parallel^{k+1} = \beta_j j_\parallel + \beta_\mathrm{i}\left(\frac{m_\mathrm{p}}{m_\mathrm{e}}A_\parallel^k - \hat{F}A_\parallel^k\right). \tag{54}$$

Some insight into the convergence property of the iterative scheme can be obtained in a shearless-slab. In Fourier space $(k_\perp, k_\parallel)$,

$$(A_\parallel^{k+1} - A_\parallel^k)_{k_\perp,k_\parallel} = \frac{\beta_\mathrm{i}\left(\frac{m_\mathrm{p}}{m_\mathrm{e}} - \hat{F}(k_\perp,k_\parallel)\right)}{k_\perp^2 + \beta_\mathrm{i}\frac{m_\mathrm{p}}{m_\mathrm{e}}}(A_\parallel^k - A_\parallel^{k-1})_{k_\perp,k_\parallel}. \tag{55}$$

Assuming uniform Maxwellian distribution for the particles, $\hat{F}(k_\parallel,k_\parallel)$ can be computed from Eq. (51) to be

$$\hat{F}(k_x,k_y,k_\parallel) = \frac{m_\mathrm{p}}{m_\mathrm{e}}\left(\frac{1}{3}\cos(k_x\Delta x) + \frac{2}{3}\right)\left(\frac{1}{3}\cos(k_y\Delta y) + \frac{2}{3}\right)\left(\frac{1}{3}\cos(k_\parallel\Delta z) + \frac{2}{3}\right). \tag{56}$$

Thus for modes with $k_x\Delta x \ll 1$, $k_y\Delta y \ll 1$, $k_\parallel\Delta z \ll 1$, the iterative scheme Eq. (54) converges rapidly. The mode with $k_x\Delta x = \pi$, $k_y\Delta y = \pi$ and $k_\parallel\Delta z = \pi$ converges slowly, with a convergence rate of $8\beta_\mathrm{i}m_\mathrm{p}/9m_\mathrm{e}(2\pi^2 + \beta_\mathrm{i}m_\mathrm{p}/m_\mathrm{e})$. However, accurate solution on the grid scale is not important, since grid-scale fluctuations are dominated by noise.

To discretize the operator $\nabla_\perp^2$ we Fourier transform in y, then discretize in x pseudo-spectrally. In the coordinates (x,y,z) the operator $\nabla_\perp^2$ is given by

$$\nabla_\perp^2 A_\parallel = \frac{\partial^2 A_\parallel}{\partial x^2}|\nabla x|^2 + 2\frac{\partial^2 A_\parallel}{\partial x\partial y}\nabla x\cdot\nabla y + \frac{\partial^2 A_\parallel}{\partial y^2}|\nabla y|^2. \tag{57}$$

For radially global simulations we set ϕ and $A_\parallel$ to zero at the radial boundaries. Suppressing the z dependence, $A_\parallel$ can be expanded as

$$A_\parallel(x,y) = \sum_{k_y} A_{\parallel,k_y}(x)\exp(\mathrm{i}k_y y) = \sum_{k_y}\exp(\mathrm{i}k_y y)\sum_{m=1}^{N_x-1} b(m,k_y)\sin\left(\frac{m\pi}{L_x}x\right), \tag{58}$$

$$b(m,k_y) = \frac{2}{N_x}\sum_{j=1}^{N_x-1} A_{\parallel,k_y}(x_j)\sin\left(\frac{jm\pi}{N_x}\right). \tag{59}$$

Substitute Eq. (59) into Eq. (58), evaluate $\nabla_\perp^2 A_\parallel$ at (x_l,y), one obtains

$$(\nabla_\perp^2 A_\parallel)(x_\mathrm{l},y) = \sum_{k_y}\exp(\mathrm{i}k_y y)\sum_{j=1}^{N_x-1} M(l,j,k_y,z)A_{\parallel,k_y}(x_j), \tag{60}$$

where the complex matrix elements $M(l,j,k_y,z)$ is given by

$$\begin{aligned} M(l,j,k_y,z) = &-\frac{2}{N_x}\sum_{m=1}^{N_x-1}\left(\left(\frac{m\pi}{L_x}\right)^2|\nabla x|^2 + |\nabla y|^2 k_y^2\right)\sin\left(\frac{jm\pi}{N_x}\right)\sin\left(\frac{lm\pi}{N_x}\right) \\ &\times\frac{2}{N_x}\sum_{m=1}^{N_x-1} 2ik_y(\nabla x\cdot\nabla y)\frac{m\pi}{L_x}\sin\left(\frac{jm\pi}{N_x}\right)\cos\left(\frac{lm\pi}{N_x}\right), \end{aligned} \tag{61}$$

where $|\nabla x|$, $|\nabla y|$ and $\nabla x\cdot\nabla y$ are evaluated at (x_l,z). The matrix M thus constructed is in general dense. The matrix to be inverted in Eq. (54) is $-M + \beta_\mathrm{i}\frac{m_\mathrm{p}}{m_\mathrm{e}}I$, which is inverted using the L–U decomposition routines provided by LAPACK. This decomposition need be constructed only once.

In general we also apply a digital filtering step along the field line after the field equations are solved. In the case of the Ampere's equation it is important to perform this filtering step after the iterative steps are completed. The point is to apply the same filtering to the first and last term on the r.h.s. of Eq. (54) and the same filtering to the $(m_\mathrm{p}/m_\mathrm{e})A_\parallel$ term on both sides. This is not the case if filtering is applied only to $A_\parallel$ at the end of each iteration.

4.2. The quasi-neutrality condition

The quasi-neutrality condition is

$$n_\mathrm{p}(x,y) + \varepsilon_g\tau\frac{V}{N}\sum_j\frac{1}{\Delta V_j}\phi(\mathbf{x}_j,t)S(\mathbf{x}-\mathbf{x}_j) = \delta n_\mathrm{i} - \delta n_\mathrm{e}. \tag{62}$$

Here $n_\mathrm{p} = \sum_{k_\perp} \frac{qn_0}{T_\mathrm{i}}(1 - \Gamma_0(b))\phi_{k_\perp} \exp(\mathrm{i}k_x x + k_y y)$ is the ion polarization density. The second term on the l.f.s. can be treated iteratively similar to the Ampere's equation. However, we found that doing so is not necessary. Replacing the term with $\varepsilon_g \tau\phi$ leads to no noticeable difference in linear simulations. Following Candy and Waltz [6], the first term can be discretized pseudo-spectrally. Let

$$\phi(x,y) = \sum_{k_y} \exp(\mathrm{i}k_y y) \sum_{m=1}^{N_x-1} b(m,k_y) \sin\left(\frac{m\pi}{L_x}x\right), \tag{63}$$

$$b(m,k_y) = \frac{2}{N_x} \sum_{i=0}^{N_x-1} \phi_{k_y}(x_\mathrm{i}) \sin\left(\frac{im\pi}{N_x}\right) \tag{64}$$

then the polarization term is given by

$$-n_\mathrm{p}(x_\mathrm{i},y) = \frac{qn_0}{T_\mathrm{i}} \sum_{k_y} \exp(\mathrm{i}k_y y) \sum_{j=1}^{N_x-1} M_\mathrm{p}(i,j,k_y,z)\phi_{k_y}(x_j), \tag{65}$$

$$M_\mathrm{p}(i,j,k_y,z) = \frac{1}{\mathrm{i}N_x} \sum_{m=1}^{N_x-1} \sin\left(\frac{jm\pi}{N_x}\right)((1 - \Gamma_0(b_+))\exp(\mathrm{i}k_+ x_\mathrm{i}) - (1 - \Gamma_0(b_-))\exp(\mathrm{i}k_- x_\mathrm{i})). \tag{66}$$

In these expressions $b_\pm$ is given by

$$b_\pm = \frac{v_{T\mathrm{i}}(x_\mathrm{i})}{\Omega_\mathrm{i}(x_\mathrm{i},z)}(k_\pm^2|\nabla x|^2 + 2k_\pm k_y \nabla x \cdot \nabla y + k_y^2|\nabla y|^2), \tag{67}$$

with $k_\pm = \pm m\pi/L_x$. The effects of variation of temperature and equilibrium magnetic field is included in this expression. As before, ∇x, ∇y are evaluated at (x_i, z).

4.3. Domain decomposition

The z direction is divided into N_z grids of equal size. These grids are used for the primary domain decomposition. Particles in each z-grid are distributed among N_s processors, so that total number of processors is $N_z N_s$. For N_y grids in the y direction, at each z there are N_y Fourier components of the electric potential ϕ, $\phi_j(x,z)$ for $k_y(j) = (j - N_y/2)2\pi/L_y, j = 0,1,\ldots,N_y - 1$. The calculation of these components are equally distributed among the N_s processors.

Due to particle free streaming along the field line, marker particles distribute uniformly along the field line in real space, which means there are more particles per poloidal angle at $\theta = 0$ than at $\theta = \pi$. For a tokamak with $R_\mathrm{maj}/a \sim 3$, this amounts to almost a factor of two difference between the number of particles in a $\theta = 0$ processor and that in a $\theta = \pi$ processor. This problem can be solved by choosing the domain size in z to be dependent on z and nonuniform grid size in z. Alternatively, we can redefine the z coordinate such that equal-sized domains in the new coordinate have equal number of particles.

Assuming particles are loaded uniform in space, the number of marker particles in $(\theta, \theta + \Delta\theta)$ is proportional to

$$\bar{J}(\theta) = \int_{r_1}^{r_2} J(r,\theta)\,\mathrm{d}r, \tag{68}$$

where r_1 and r_2 are the inner and outer boundaries of the simulation domain. This number depends on θ for fixed $\Delta\theta$, or fixed $\Delta z = q_0 R_\mathrm{maj}\Delta\theta$. We can define $z'(\theta)$ so that the number of particles in $(z', z' + \Delta z')$ is independent of θ. This is accomplished by choosing

$$\frac{\mathrm{d}z'}{\mathrm{d}\theta} = 2\pi_0 R_\mathrm{maj} \frac{\bar{J}(\theta)}{\oint \bar{J}(\theta)\,\mathrm{d}\theta}. \tag{69}$$

This choice of z' also makes the parallel box size invariant, $z'(\theta = \pi) - z'(\theta = -\pi) = 2\pi q_0 R_\mathrm{maj}$.

5. Examples of numerical simulation

The GEM code has been extended to include general tokamak equilibrium geometry, arbitrary density and temperature profiles, and arbitrary number of minority ion species. In this section some examples of GEM simulation are presented. All simulations are with $m_\mathrm{p}/m_\mathrm{e} = 1837$ and $m_\mathrm{i}/m_\mathrm{p} = 1$.

5.1. Effect of flux surface shape on the linear growth rate

The effect of flux surface shape on ITG mode growth rate has been studied using local, ballooning formalism [14,15]. Growth rate is found to decrease with increasing elongation. Here we present simulation results which show similar effects of elongation on the growth rate. This serves as a benchmark for the implementation of general geometry in GEM. Since GEM is global in radius, care must be taken to avoid density and temperature profile effect on the mode, when comparing GEM simulation with local analysis. In the following we first set $\kappa_n = -\frac{1}{n}\frac{\mathrm{d}n}{\mathrm{d}r} = 0.0039$ and $\kappa_T = -\frac{1}{T_\mathrm{i}}\frac{\mathrm{d}T_\mathrm{i}}{\mathrm{d}r} = 0.0117$, and then set $n(r) = n_0$, $T_\mathrm{i}(r) = T_\mathrm{e}(r) = T_0$. The elongation and triangularity profiles are given by

$$\kappa(r) = \kappa_0 + \kappa'(r - r_0), \tag{70}$$

$$\delta(r) = \delta_0 + \delta'(r - r_0). \tag{71}$$

The safety factor is given by a linear profile

$$q(r) = q_0 + q'(r - r_0). \tag{72}$$

With $q_0 = 2$, $q' = 0.01557$, $a = 256.92$, $r_0 = 128.46$ thus $\hat{s} = 1$ at r_0, $R_\mathrm{maj} = 770.76$, Other parameters are: $R_0'(r) = 0$, $\beta_\mathrm{i} = 0$, $\nu_\mathrm{ei} = 0$. These parameters are chosen so that the local parameters at $r = r_0$ match the case studied by Waltz and Miller [15]. The function f in Eq. (1) is given by

$$f(r) = R_\mathrm{maj} + f'(r - r_0), \tag{73}$$

so that on the reference surface r_0 the toroidal field is given by R_maj/R. This amounts to choosing the toroidal field at $R = R_\mathrm{maj}$ on the reference flux surface r_0 as the unit for the magnetic field. Simple linear profiles are used in Eqs. (70)–(73) because profile effect is to be avoided, and the radial domain size L_x is to be chosen so that κ, δ and q do not deviate significantly from values at r_0. On the other hand, L_x should be large enough to avoid boundary effects. For linear simulations in this paper we choose $L_x = 49\rho_\mathrm{i}$. We have verified that choosing $L_x = 35\rho_\mathrm{i}$ does not cause significant change in the results. Once $q'(r_0)$ and $\Psi(r_0)$ are known (Eq. (4)), f' is determined in the Miller equilibrium model, through [9]

$$\frac{\mathrm{d}q}{\mathrm{d}\Psi} = \frac{f'}{f}q + \frac{f}{2\pi}\oint \frac{1}{R_s^3 B_{ps}^2}\left(\frac{2}{R_c} - \frac{2\sin u}{R_s} + \frac{ff'}{R_s B_{ps}} + \beta_\mathrm{i}\frac{R_s}{B_{ps}}p'\right)\mathrm{d}l. \tag{74}$$

Here $R_s(l)$ and $Z_s(l)$ are a parameterization of the flux surface at r_0, with l the poloidal arc length. The angle u and radius of curvature R_c are defined through $\mathrm{d}R_s/\mathrm{d}l = \cos u$, $\mathrm{d}Z_s/\mathrm{d}l = \sin u$ and $\mathrm{d}u/\mathrm{d}l = 1/R_c$. Note that f' is constant on the r_0 surface, hence Eq. (74) can be easily solved numerically.

Waltz and Miller (WM) studied the effect of shaping on the $k_y\rho_s = 0.4$ mode, with $\rho_s = c_s/(eB_\mathrm{unit}/m_\mathrm{i})$ and $B_\mathrm{unit} = q_0\Psi'(r_0)/r_0$. The quantity B_unit is roughly proportional to κ, therefore the mode number $k_y\rho_\mathrm{i}$ varies as κ and δ are changed, while $k_y\rho_s$ is fixed. For concentric elliptic surfaces $\rho_\mathrm{i} \approx \kappa\rho_s$.

Figs. 2–4 show the simulations results. The dotted lines in Figs. 2 and 4 are estimated from Fig. 3(b) and (c) of Ref. [15]. GEM data show similar effects of elongation (square points in Fig. 2), in reasonable agreement with the WM data. The effect of elongation with fixed $k_y\rho_\mathrm{i}$, i.e. fixed toroidal mode number $n = k_y r_0/q$, is shown in Fig. 3. The strong stabilization effect of elongation observed is in agreement with previous studies [16,14]. Notice that at large κ the unstable spectrum shifts toward high k_y. This feature can be understood as a Finite–Larmor–Radius (FLR) effect. The perpendicular wave number is given by

$$k_\perp^2 = k_x^2|\nabla x|^2 + k_y^2|\nabla y|^2 + k_x k_y \nabla x \cdot \nabla y. \tag{75}$$

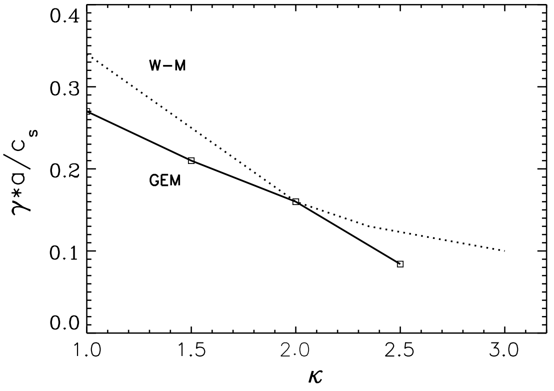

Fig. 2. Linear growth rate vs. elongation for fixed $k_y\rho_s = 0.4$, compared with Waltz–Miller results.

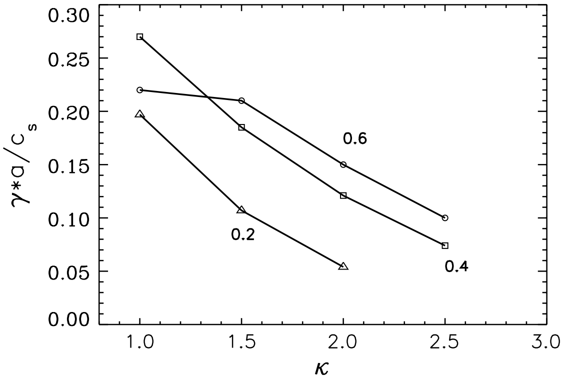

Fig. 3. Linear growth rates vs. elongation for fixed $k_y\rho_i$.

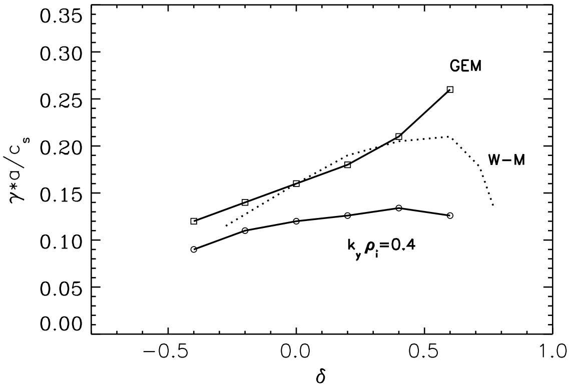

Fig. 4. Linear growth rates vs. triangularity.

For a ballooning mode with the ballooning angle $\theta_0 = 0$, $k_x = 0$ at $\theta = 0$, hence $k_\perp \approx k_y|\nabla y| \approx \frac{r_0}{q_0}\hat{q}(r,0)\nabla\theta$. The elongation reduces $k_\perp$ near $\theta = 0$ through reducing $\nabla\theta$, a geometrical effect. Finite–Larmor–Radius stabilization is therefore reduced.

Fig. 4 shows the effect of triangularity on the $k_y\rho_s = 0.4$ mode. GEM results (square points) are again in reasonable agreement with the WM data, showing a strong effect of triangularity. However, the results for the $k_y\rho_i = 0.4$ mode show weaker effect of triangularity. For fixed $k_y\rho_s = 0.4$ GEM simulations show continuous increase in γ as δ increases, while the WM data show a decrease at large δ. Because the radial dependence of $\kappa(r)$ ($\delta(r)$) is chosen such that κ' (δ') is proportional to κ_0 (δ_0), profile effect becomes more important at large κ (δ). We also note that with the above specification for the surface shapes, singularity occurs in ∇r and $B_p(r,\theta)$ at large δ ($\delta > 0.8$). Due to these reasons, comparison between GEM simulation and the local, ballooning calculations becomes more inconclusive at large δ. However, this does not seem to explain the discrepancy between GEM data and the WM data at $\delta = 0.6$, since choosing $L_x = 35\rho_i$ yields the same growth rate for $\delta_0 = 0.6$ as choosing $L_x = 50\rho_i$ in GEM simulations.

5.2. Nonlinear electromagnetic simulation

Here we present examples of nonlinear simulations, and briefly assess the issue of whether noise affects the nonlinear stage in the simulation model presented here. The density profile is assumed to be linear with $\rho_i/L_n = 0.0021$. The temperature profile is

$$\frac{T(s)}{T(s_0)} = \exp\left(-\frac{a\Delta s}{L_T}\tanh\frac{s-s_0}{\Delta s}\right), \tag{76}$$

with $s = r/a$, $a = 256.92\rho_i$, $L_T = 150\rho_i$, $s_0 = 0.5$, $\Delta s = 0.6$. The q-profile is given by

$$q(s) = 1 + 0.43236s^2 + 2.33528s^3. \tag{77}$$

We also assume $f(\Psi) = R_{\mathrm{maj}}$ in Eq. (1), and take $B = B_T$. As discussed in Section 1, these equilibrium quantities are defined numerically in an equilibrium module. Simple forms are assumed here for the purpose of illustrating some numerical properties of nonlinear simulations. The magnetic surface shape is given by $\delta = 0.2$, $\kappa = 1.3$, $R_0' = -0.1$. Other parameters are: $\beta = 0.012$, $L_x = 90\rho_i$, $L_y = 64\rho_i$, $(N_x, N_y, N_z) = (128, 64, 32)$, $\omega_{ci}\Delta t = 2$, $\nu_{ei} = 10^{-4}$. The split-weight parameter is $\varepsilon_g = 0.1$. A convergence test with respect to particle number is carried out, with 32, 64 and 128 number of particles per spatial cell per species. The evolution of ion heat diffusivity (which is essentially the total flux in the entire simulation domain, normalized with the parameter L_T and L_n) for the three simulations is shown in Fig. 5. The case with 64/cell is virtually identical with the 128/cell case for $tv_{Ti}/a < 150$. We note that no attempt is made to adjust the temperature and density profiles used in the equilibrium distribution of the δf method, therefore density and temperature relaxation occurs in the long-term, which is a possible explanation for the long time slow decrease in the ion heat flux. Nevins et al. [17] recently suggests that discrete particle noise in δf particle simulations could accumulate in time and eventually lead to the suppression of turbulence. To assess whether particle noise plays an important role

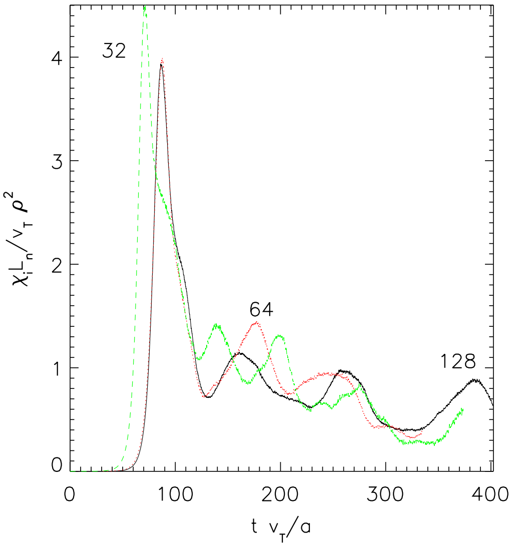

Fig. 5. Evolution of ion heat flux for three simulations with different number of particles.

in the later stages of these simulations, an estimate of the noise induced ion heat diffusivity is needed. Since the noise is dominated by high frequency, short wave length component, the noise induced flux can be observed by randomizing the particle y coordinates (while keeping all other information in the simulation) and observe the fluxes on a time scale shorter than the ITG growth time. We have carried out such tests for the case here but with $N_y = 32$, 32 particles/cell, and verified that the noise induced fluxes are proportional to the square of the mean magnitude of weights. Thus the noise induced flux for the initial particle weights is just the observed ion heat flux during the initial stage of the simulation, $\omega_{ci}t < 2000$ ($\gamma_{max}/\omega_{ci} = 3.6 \times 10^{-4}$), which is $\chi_{noise}(0)L_n/v_{Ti}^2\rho_i^2 \sim 4 \times 10^{-5}$ for an initial average weight of $|w| = 0.005$. A measure of the noise level in χ_i at later times is given by $\chi_{noise}(t) = \chi_{noise}(0)|w|^2(t)/|w|^2(0)$. Fig. 6 plots the evolution of the ion and electron average weights, together with this measure of the noise in χ_i, based on the electron weight, which is larger than the ion weights in later times. Near the end of the simulation, $v_{Ti}t/a > 300$, $\chi_{noise}L_n/v_{Ti}\rho_i^2 < 0.003$, very small compared with the observed flux $\chi_i L_n/v_{Ti}\rho_i^2 \sim 1$. The electron heat flux (only the case with 32/cell in Fig. 5 is shown in Fig. 7) is ~1/4 of the ion heat flux, which is still over 50 times larger than the noise level. We therefore conclude that discrete particle noise plays little role in the simulation with 128 particles per cell, up until the end of the simulation. For the case with 32/cell the noise level is roughly increased by 4 times, and the electron flux indeed appears more noisy near the end of the simulation (Fig. 7), nevertheless, there appears to be no significant change in χ_e, averaged over the fast oscillations.

It is clear that as the simulation continues, eventually noise will grow to large values to dominate the simulation. Increasing the number of particles will only postpone this stage. That the particle weights continue to grow in an apparent steady state turbulence is a long-standing issue [18] in δf simulations. In collisionless simulations (as is the case for the ion species here) this continuous growth of the weight is a result of the turbulent diffusion of test particles. With collisions the phase space granulation process is eventually balanced by collisional processes, which limit the magnitude of the physical distribution function (δf), but not the particle weights in the commonly used collisional algorithm [19] in which Monte-Carlo techniques are used for the diffusive collisional processes. This is shown in Fig. 7. A simulation of the case with *32*/cell is repeated except with $\nu_{ei} = 0$. It can be seen that the two cases are identical linearly and yield about the same level of χ_e. However, the average electron weight grows faster in the nonlinear stage in the collisional case. Thus the commonly used collisional algorithm in δf simulations does not suppress the weights from growing, even if the process of phase space granulation is suppressed by collisions at sufficiently fine scales. The fundamental reason of this is that with collisions δf is better regarded as the integral of the particle weights at a given phase space location [19]. It is perfectly reasonable and normally true that δf is limited by collisions but the weights distribution continues to broaden. This observation is crucial for future development of algorithms for long-term simulations. To achieve arbitrarily long-term steady state it is necessary to control the long-term growth of the par-

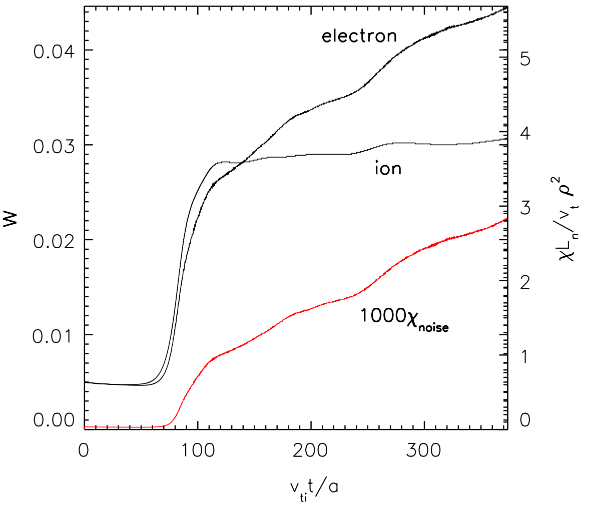

Fig. 6. Evolution of average magnitude of electron and ion weights (labeled with "electron" and "ion"), and estimate of the noise-induced ion heat flux ($1000\chi_{noise}$).

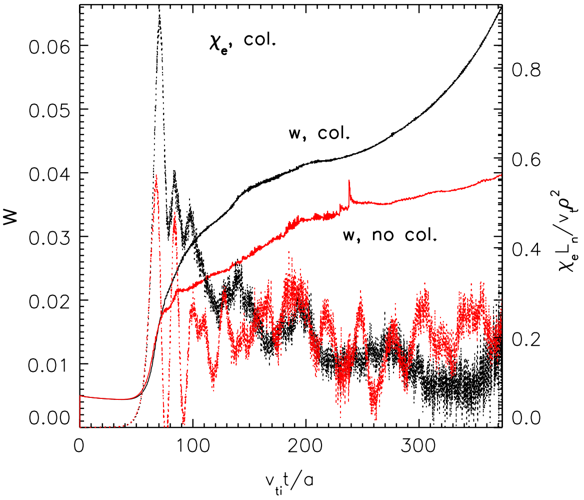

Fig. 7. Evolution of the average magnitudes of the electron weight with/without e–i collisions, and the electron heat flux.

ticle weights, yet in doing so the important kinetic information due to test particle turbulent diffusion (which leads to the weight growth as a true physical process) must be retained. Many of the subtleties involved in a near-collisionless steady state turbulence, such as the role of the vanishing dissipation, entropy production and the generation of fine phase-space scales due to $E \times B$ nonlinearity, are discussed by Krommes and Hu [18]. A scheme for controlling the weights is successful only by discarding some of the kinetic information contained in the distribution, as is true both in Krommes' "Thermostatted δf" [20] and the Particle-Continuum method [21]. Before that can be done, there is an important task of assessing the relevance of the discarded information numerically, particularly in the presence of magnetic field perturbations, which could enhance turbulent diffusion and phase-space granulation for the electron distribution function. We will report results of such numerical studies in a future publication.

6. Summary

We have described the implementation of general equilibrium profiles and flux-surface shapes in the GEM code. Various quantities, such as the magnitude of the magnetic field, the Jacobian, etc. are defined numerically, so arbitrary axisymmetric equilibrium can be handled. The field equations are Fourier transformed in the toroidal direction, then discretized in the radial direction pseudo-spectrally. An analysis of the split-weight scheme is given, which suggests that the split-weight scheme achieves better numerical stability by enforcing the equation for the rate of change of the electric potential, which is not compatible with the quasi-neutrality condition for grid-scale fluctuations, to be satisfied. The issues of long-term weight growth and discrete particle noise are briefly discussed.

Acknowledgments

We thank Dr. Jeff Candy for helpful discussion on the use of the Miller equilibrium model for the linear simulations in this paper. We are grateful for support from the US Department of Energy, Office of Fusion Energy Sciences. Work is part of the DOE Scientific Discovery through Advanced Computing, the Center for Gyrokinetic Plasma Simulation.

References

[1] Y. Chen, S. Parker, A delta-*f* particle method for gyrokinetic simulations with kinetic electrons and electromagnetic perturbations, J. Comput. Phys. 189 (2003) 463.

[2] R. Sydora, V. Decyk, J. Dawson, Fluctuation-induced heat transport results from a large global 3d toroidal particle simulation model, Plasma Phys. Controlled Fusion 38 (1996) A281.
[3] Y. Chen, S.E. Parker, Gyrokinetic turbulence simulations with kinetic electrons, Phys. Plasmas 8 (2001) 2095.
[4] J. Cummings, Ph.D. thesis, Plasma Physics Lab, Princeton University, 1994.
[5] W. Dorland, F. Jenko, M. Kotschenreuther, B. Rogers, Electron temperature gradient turbulence, Phys. Rev. Lett. 25 (2000) 5579.
[6] J. Candy, R. Waltz, An Eulerian gyrokinetic–Maxwell solver, J. Comput. Phys. 186 (2003) 545.
[7] B. Cohen, A. Dimits, Implicit, partially linearized, electromagnetic particle simulation of plasma drift-wave turbulence, Phys. Rev. E 56 (1997) 2151.
[8] J. Reynders, Gyrokinetic simulation of finite-β plasmas on parallel architectures, Ph.D. Thesis, Princeton University, 1992.
[9] R.L. Miller, M.S. Chu, J.M. Greene, Y.R. Lin-Liu, R.E. Waltz, Noncircular, finite aspect ratio, local equilibrium model, Phys. Plasmas 5 (1999) 973.
[10] M.A. Beer, S.C. Cowley, G.W. Hammett, Field-aligned coordinates for nonlinear simulations of tokamak turbulence, Phys. Plasmas 2 (1995) 2687.
[11] W. Lee, Gyrokinetic particle simulation model, J. Comput. Phys. 72 (1987) 243.
[12] T.S. Hahm, Nonlinear gyrokinetic equations for turbulence in core transport barriers, Phys. Plasmas 3 (1996) 4658.
[13] I. Manuilskiy, W.W. Lee, The split-weight particle simulation scheme for plasmas, Phys. Plasmas 7 (2000) 1381.
[14] D.D. Hua, X.Q. Xu, T.K. Fowler, Ion-temperature-gradient modes in noncircular tokamak geometry, Phys. Fluids B 4 (1992) 3216.
[15] R. Waltz, R.L. Miller, Ion temperature gradient turbulence simulations and plasma flux surface shape, Phys. Plasmas 6 (1999) 4265.
[16] G. Rewoldt, W.M. Tang, M.S. Chance, Electromagnetic kinetic toroidal eigenmodes for general magnetohydrodynamic equilibria, Phys. Fluids 164 (1982) 480.
[17] W.M. Nevins, G.W. Hammett, A.M. Dimits, W. Dorland, D.E. Shumaker, Discrete particle noise in particle-in-cell simulations of plasma microturbulence, Phys. Plasmas 12 (2005) 122305.
[18] J. Krommes, G. Hu, The role of dissipation in the theory and simulations of homogeneous plasma turbulence, and resolution of the energy paradox, Phys. Plasmas 1 (1994) 3211.
[19] Y. Chen, R.B. White, Collisional δf method, Phys. Plasmas 10 (1997) 3591.
[20] J.A. Krommes, Thermostatted δf, Phys. Plasmas 6 (1999) 1477.
[21] S. Vadlamani, S.. Parker, Y. Chen, C. Kim, The particle-continuum method: an algorithmic unification of particle-in-cell and continuum methods, Comp. Phys. Comm. 164 (2004) 209.